JVI Journals.ASM.org

Structure and Dynamics of Adeno-Associated Virus Serotype 1 VP1-Unique N-Terminal Domain and Its Role in Capsid Trafficking

Balasubramanian Venkatakrishnan,[a]* Joseph Yarbrough,[a] John Domsic,[a]* Antonette Bennett,[a] Brian Bothner,[b] Olga G. Kozyreva,[c] R. Jude Samulski,[c] Nicholas Muzyczka,[d] Robert McKenna,[a] Mavis Agbandje-McKenna[a]

Department of Biochemistry and Molecular Biology, College of Medicine, University of Florida, Gainesville, Florida, USA[a]; Department of Chemistry and Biochemistry, Montana State University, Bozeman, Montana, USA[b]; Department of Pharmacology, Gene Therapy Center, University of North Carolina at Chapel Hill, Chapel Hill, North Carolina, USA[c]; Department of Molecular Genetics and Microbiology and Powell Gene Therapy Center, College of Medicine, University of Florida, Gainesville, Florida, USA[d]

The importance of the phospholipase A_2 domain located within the unique N terminus of the capsid viral protein VP1 (VP1u) in parvovirus infection has been reported. This study used computational methods to characterize the VP1 sequence for adeno-associated virus (AAV) serotypes 1 to 12 and circular dichroism and electron microscopy to monitor conformational changes in the AAV1 capsid induced by temperature and the pHs encountered during trafficking through the endocytic pathway. Circular dichroism was also used to monitor conformational changes in AAV6 capsids assembled from VP2 and VP3 or VP1, VP2, and VP3 at pH 7.5. VP1u was predicted (computationally) and confirmed (in solution) to be structurally ordered. This VP domain was observed to undergo a reversible pH-induced unfolding/refolding process, a loss/gain of α-helical structure, which did not disrupt the capsid integrity and is likely facilitated by its difference in isoelectric point compared to the other VP sequences assembling the capsid. This study is the first to physically document conformational changes in the VP1u region that likely facilitate its externalization from the capsid interior during infection and establishes the order of events in the escape of the AAV capsid from the endosome en route to the nucleus.

Adeno-associated viruses (AAVs) are nonpathogenic members of the *Parvoviridae* family, belong to the *Dependovirus* genus, and require helper functions from viruses such as *Adenovirus* or *Herpesvirus* for infection (1–4). Twelve distinct AAV serotypes and over 100 genome isolates have been reported (5–7). Considerable interest has been generated in their development as gene delivery vectors, and numerous studies show that each virus has unique cellular transduction characteristics (5, 8–13). Recent successes in AAV gene delivery, including the treatment of blindness using AAV2 (14), highlight the clinical potential of these vectors and generated a considerable amount of media and public interest in the use of AAV vectors. However, many key questions remain to be answered about the basic biology of these viruses during infection, including the role of capsid viral protein (VP) transitions that enable infection. Understanding such processes can aid development of more-efficacious forms of the AAVs as vectors for gene delivery.

The AAVs package a genome of ~4.7 kb in an icosahedral capsid (T = 1), assembled from 60 capsid VP monomers, with a diameter of ~260 Å. The capsid is comprised of three VPs: VP1, VP2, and VP3. VP1 contains the entire VP2 sequence in addition to a unique ~137-amino-acid N-terminal region (VP1u), while the VP2 protein contains the entire VP3 sequence in addition to an ~65-amino-acid N-terminal region (VP1/2 common region). VP3 is the major capsid protein, accounting for approximately 50 of the 60 capsid monomers, while there are approximately 5 copies each of VP1 and VP2 (and thus a ratio of 1:1:10 for VP1:VP2:VP3) per capsid as determined by gel densitometry studies (15–17). The three-dimensional structures for several AAV serotypes including AAV1, AAV2, AAV3b, AAV4, AAV5, AAV6, AAV7, AAV8, and AAV9 have been determined by cryoelectron microscopy (cryo-EM) and image reconstruction and/or by X-ray crystallography (18–26, 71).

The structure of only the common C-terminal VP3 region (~530 residues) is known in atomic detail. Cryo-EM studies of AAV1, AAV2, and AAV4 capsids identified density "globules" located in the interior of the capsid beneath the icosahedral 2-fold axis, which have been interpreted as the N-terminal regions of VP1 and VP2 (23, 27, 28), but the structural topology of these regions remains to be elucidated. In crystal structures, the locations of VP1u, the VP1/2 common region, and the first ~15 residues of VP3 have not been observed. This is proposed to be due either to low copy numbers of VP1 and VP2 in the capsids or to the possibility that the N termini of VP1, VP2, and VP3 adopt different conformations in the capsid. These properties are incompatible with the icosahedral symmetry assumed during structure determination.

The structural topology of the common AAV VP3 region is highly conserved. It consists of a core eight-stranded antiparallel β-barrel (designated βB-βI) with an additional β-strand A (βA) that forms the contiguous capsid shell, while loop insertions between the strands form the majority of the capsid surface (Fig. 1A). The loops contain small stretches of helical and β-strand structure as well as variable regions (VRs, as defined in reference 71) when different AAV structures are compared. The major capsid surface features include depressions at the icosahedral 2-fold symmetry

Received 15 September 2012 **Accepted** 1 February 2013

Published ahead of print 20 February 2013

Address correspondence to Robert McKenna, rmckenna@ufl.edu, or Mavis Agbandje-McKenna, mckenna@ufl.edu.

* Present address: Balasubramanian Venkatakrishnan, Department of Molecular & Cellular Biochemistry, Indiana University, Bloomington, Indiana, USA; John Domsic, The Wistar Institute, Philadelphia, Pennsylvania, USA.

doi:10.1128/JVI.02524-12

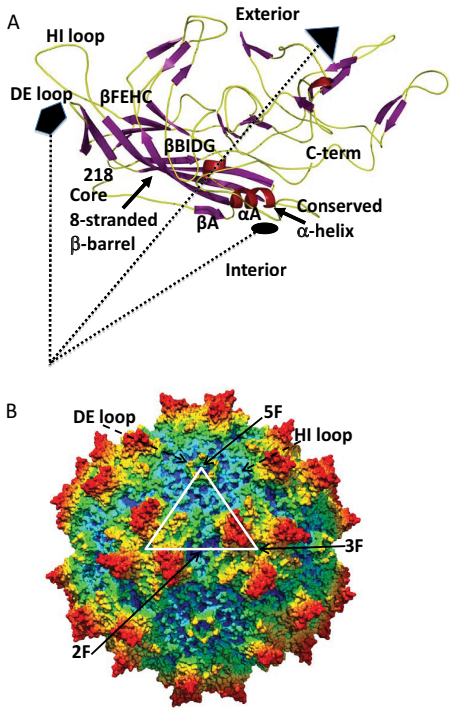

FIG 1 AAV1 structure. (A) Crystal structure of AAV1 capsid VP3 monomer (PDB ID, 3NG9). The β-strands are shown in purple ribbon, the conserved α-helix A is in red, and loops between the strands are in yellow. The dotted lines show the relative positions of the 5-fold (filled pentagon), 3-fold (filled triangle), and 2-fold (filled oval) interfaces of symmetry from the center of the capsid. An eight-stranded β-barrel (with β-sheets βCHEF and βBIDG), along with βA (labeled) and α-helix A (αA), forms the core of the VP monomer structure, flanked by large loop regions. The DE and HI loops (between β-strands D and E and between H and I, respectively) as well as the first ordered N-terminal residue (218), the C-terminus, and the interior and exterior capsid surfaces are labeled. (B) Radially color-cued (from capsid center to surface, blue to green to yellow to red) surface representation of the AAV1 capsid. The white triangle depicts a viral asymmetric unit bounded by one 5-fold axis and two 3-fold axes with a 2-fold axis between them. The approximate locations of the icosahedral 2-fold (2F), 3F, and 5F axes are indicated by the black arrows. The positions of the DE and HI loops are indicated by the dashed arrows. Images in panels A and B were generated using PyMol (DeLano Scientific) and UCSF-Chimera (70), respectively.

axis and surrounding the 5-fold axis and protrusions surrounding the 3-fold axes (Fig. 1B). A conserved α-helix (αA, residues 294 to 303; AAV1 VP1 numbering) forms the wall of the 2-fold depression (Fig. 1A). The 3-fold protrusions are formed from intertwining loops from 3-fold symmetry-related VP3 monomers and are the most variable regions within parvovirus capsids with respect to sequence and structure. Two small stretches of β-strand structure, between βD and βE, form a radial β-ribbon at the 5-fold icosahedral axis (Fig. 1A). Five such ribbons form a conserved cylindrical channel connecting the interior to the exterior of the capsid (Fig. 1B). A structurally conserved loop between βH and βI (HI loop) (Fig. 1A) forms the most extensive 5-fold related VP contacts and lies on the depression surrounding the channel (Fig. 1B).

The infectious pathway of the AAV is initiated by the attachment of the virus to the cell surface by binding to a primary glycan receptor (11, 13, 29–35). This is followed by interactions with membrane-bound coreceptors, for example, fibroblast growth factor receptor and αVβ5 and α5β1 integrin receptors for AAV2 (36–38), platelet-derived growth factor receptor for AAV5 (39), and the 37-/67-kDa laminin receptor for AAV8 (40). Following attachment, the endocytosis of the capsid has been reported to occur by means of clathrin-coated pits (41), though recent studies have described a clathrin-independent mechanism (42). After endocytosis, the virus traffics through the endocytic pathway and accumulates in the perinuclear region (43) before delivering its infective genome to the nucleus. However, the exact mechanism of endosomal escape and nuclear entry remains to be fully elucidated. It has been reported that shortly after entering the early endosome, the N termini of VP1 and VP2 become externalized on the capsid surface while the capsid remains assembled (44). It is known that VP1u contains a phospholipase A_2 domain (PLA_2) and two nuclear localization signals (NLSs) that modify the endosomal membranes to enable escape and targeting to the nucleus, respectively. Genetic studies show that both PLA_2 and NLS are necessary for efficient infection (44–48). It is also known that the acidic environment of the endosome is essential for virus infection, as inhibitors of the vacuolar H^+-ATPases such as bafilomycin A1 and treatment of cells with NH_4Cl both inhibit AAV transduction and reduce trafficking to the nucleus (49–53). However, VP1u was not detected on the capsid surface after treatment of particles with the acidic pHs (~pH 5.0) of the endosome alone (44). Therefore, the exact trigger of VP1u externalization, which is common to all parvoviruses, is unclear and requires further investigation.

In this study, computational and biophysical approaches were used to characterize the structural features of the AAV VP1 in the context of the capsid. The monomer sequence was analyzed to identify possible regions of intrinsic disorder, and the isoelectric point (pI) values of the three VP sequences, VP1, VP2, and VP3, were calculated. The VP1u and VP3 common sequences were predicted to adopt a structured state, while the VP1/VP2 common region displayed a high probability of being intrinsically disordered. The pI value for VP1u was lower than that of the overall capsid, suggesting differential susceptibility to environmental conditions, such as those encountered in the endosome. Circular dichroism (CD) confirmed that the VP1u in AAV1 and AAV6 has an ordered α-helical secondary structure in solution. This α-helical structure was gradually lost with decrease in pH from 7.5 to 4.0 and was restored when the pH was returned to 7.5, highlighting a transition likely associated with function. Negative-stain EM visualization showed that AAV1 capsids remain intact during pH treatment, consistent with previous reports of structural integrity for AAV8 capsids incubated at the pHs associated with the endocytic pathway and characterized by X-ray crystallography (54). This study is the first to physically document conformational changes in the VP1u region and establishes the order of events in the escape of the AAV capsid from the endosome en route to the nucleus.

MATERIALS AND METHODS

VLP expression and purification. Sf9 cells infected with a baculovirus construct containing the AAV1 *cap* gene, expressing VP1, VP2, and VP3, was used to produce virus-like particles (VLPs) and purified as previously reported (19). In addition, two types of AAV6 VLPs, assembled from VP2 and VP3 only or VP1, VP2, and VP3, were produced from a baculovirus construct containing the AAV6 *cap* gene expressing VP2 and VP3 (22) or by a double infection with a construct containing the *cap* gene expressing

VP1 and a second construct containing the *cap* gene expressing VP2 and VP3. Briefly, cells grown in Erlenmeyer flasks at 300 K using Sf-900 II SFM medium (Gibco/Invitrogen Corporation) were infected with the respective baculovirus constructs at a multiplicity of infection of 5.0 PFU per cell. The cells were lysed, 72 h postinfection, by three freeze-thaw cycles with Benzonase added after the second cycle. The sample was centrifuged at 12,100 × *g* at 4°C for 15 min to separate the VLPs from the cell debris. The VLPs were pelleted by sucrose cushion (20% [wt/vol] sucrose in 50 mM Tris-HCl, 100 mM NaCl, 1 mM EDTA, and 0.2% Triton X-100) centrifugation at 149,000 × *g* at 4°C for 3 h. The pellet was further purified by sucrose gradient (10 to 40% [wt/vol] sucrose in 25 mM Tris-HCl, 100 mM NaCl, 0.2% Triton X-100, and 2 mM $MgCl_2$) centrifugation at 151,000 × *g* at 4°C for 3 h. The sample purity and integrity were monitored by 10% SDS-PAGE with Coomassie blue staining and electron microscopy (50,000×), respectively, and the concentration was determined using UV/visible light (Vis) spectrometry (260/280 nm; molar extinction coefficient, 1.7 for concentration in mg/ml). The purified samples were buffer exchanged into phosphate-citrate buffers (with 150 mM NaCl) using specific ratios of 0.2 M Na_2HPO_4 and 0.1 M citrate to achieve a final pH of 7.5 or pH 6.0, 5.5, and 4.0 for the low-pH studies described below.

Empty-capsid production and purification. Empty capsids of AAV6, assembled from VP1, VP2, and VP3, were produced in HEK293 cells. A 5-liter suspension culture, at an initial concentration of 1×10^6 cells/ml, was transfected with two plasmids, pXX680 (carrying Ad helper genes) and pXR6 (encoding VP1, VP2, and VP3 of AAV6), for 48 h as previously described (55). The cell pellet was resuspended in phosphate-buffered saline (PBS) and purified as described above for the baculovirus-expressed VLPs.

VLP and empty-capsid secondary-structure analysis. The secondary-structure state of the AAV1 VLPs (assembled from VP1, VP2, and VP3) was analyzed at different pHs and increasing temperatures using CD. The AAV6 VLPs (assembled either from VP2 and VP3 or from VP1, VP2, and VP3) and empty capsids (assembled from VP1, VP2, and VP3) were also analyzed at pH 7.5 by CD. All the CD experiments were carried out on an Aviv model 410 circular dichroism spectrometer. Preliminary analysis showed that CD data collection below a wavelength of 200 nm drastically overloaded the dynode and created large variations in the data accompanied by large error values. Therefore, all the data were collected at a wavelength range of 260 to 200 nm. Data were collected with sample concentrations of 0.4 mg/ml in quartz cuvettes with 350-μl volumes at a 1-mm path length. A single scan was collected for every wavelength (total, 61 scans), and results were averaged over a 5-s exposure time. The pH 7.5, 6.0, 5.5, and 4.0 studies were conducted in triplicate with 50 scans per experimental run at 30°C. Experiments that measured the thermal transition temperatures of the VLPs were also done in triplicates with CD spectra collected at a temperature range of 30 to 90°C with three-degree intervals (21 spectra).

Standard CD deconvolution programs require data collected to at least 190 nm; therefore, these programs could not be used to deconvolute the data collected between 260 and 200 nm. Thus, an in-house algorithm was developed by utilizing CD information for pure α-helix, β-sheet, and random coil structures of polylysine from data published by Greenfield and Fasman (56). An array of CD spectra corresponding to theoretical combinations of α-helix, β-sheet, and random coil between 0 and 100% with 10% intervals was generated for comparison to the experimental observations. To analyze the experimental data, each spectrum was first scaled to the theoretical CD spectra (by wavelength) and then fitted by a least-squares approach.

AAV capsid integrity. The AAV1 capsid integrity following temperature and pH treatment was checked by negative-stain EM studies. Five microliters of sample was applied to carbon-coated copper grids and incubated for 5 min. The sample drop was wicked (Whatman filter paper) and washed with double-distilled water (ddH_2O), and the grid was negatively stained with 5 μl Nano-W (Nanoprobes) for 1 min and examined in a JEOL 1200 EX transmission electron microscope at a magnification of ×50,000.

Computational analysis of the AAV VP sequence and structure. The ExPASy Compute pI/M_w tool (57) was used to calculate pI values for the VP1u, VP1/2 common region, and VP3 sequences for the 12 AAV serotypes characterized to date (5–7). The values obtained were subsequently used to calculate the pI values for the entire capsids (60 VPs) based on a VP1:VP2:VP3 ratio of 1:1:10 using an algorithm developed in-house. Based on an accepted pI value of ~5.0 for nucleotides (58), the pI value was also calculated for capsids packaged with genomic DNA (4.7 kb). To evaluate the order/disorder potential for the AAV VPs, the PONDR-Fit program (59) was used to calculate the intrinsic disorder disposition for the VP1 sequence of AAV1, AAV2, AAV5, and AAV8, selected to represent the range of sequences similar among the AAVs and for which high-resolution crystal structures are available (at least for the VP3 common region) and can be used for validation. Predicted models (a total of five) for the first 250 amino acids of AAV1 VP comprising the VP1u, the VP1/VP2 common region, and the first 48 residues of the VP3 common region were generated using the Robetta full-chain protein structure prediction server (60). The Coot (61) program was used to superpose the models onto the available crystal structures of bovine pancreatic phospholipase A_2 (62) (Protein Data Base [PDB] ID, 1BP2) and AAV1 (PDB ID, 3NG9), using a least-squares-based secondary structure matching (SSM) subroutine, for comparative analysis.

RESULTS

Computational analysis predicts an ordered structure for VP1u but intrinsic disorder for the VP1/2 common region of the AAV capsid VP. Five Robetta server models generated for the N-terminal 250 amino acids of AAV1 predicted that the VP1u sequence (residues 1 to 137), not observed in the crystal structure, contain several α-helical segments connected by loop regions (Fig. 2). The VP1/2 common region (residues 138 to 202), however, consisted mainly of random coil (loop) secondary structure (Fig. 2C and D). A superposition of the best two models onto the bovine pancreatic phospholipase A_2 structure (root mean square deviations [RMSDs], 3.3 and 2.8 Å) is shown in Fig. 2C. The two dominant helices that included the PLA_2 active site showed a high degree of overlap between the structures. Superposition of these VP1u models onto the crystal structure of the AAV1 capsid monomer, guided by the structures of residues 217 to 250 present in both the models and the crystal structure, localized the VP1u directly beneath the icosahedral 2-fold interface (Fig. 2D) in the capsid interior.

The PONDR-Fit algorithm predicted an ordered structure for the VP1u sequence, an intrinsically disordered (threshold value, <0.5 [59]) stretch in the VP1/2 common region (residues ~140 to 202) and up to residue ~220 in the VP1/VP2/VP3 common sequence and an ordered structure for the remainder of the common VP3 sequence with small stretches of intrinsic disorder within the previously defined capsid VRs (Fig. 3). The consensus low-intrinsic-disorder disposition regions predicted for VP3 were localized to the structurally conserved βA-βI and αA regions (Fig. 3).

The calculated pI values for the VPs of AAV1 to AAV12 are plotted in Fig. 4. The VP1u region had a consistent acidic pI value of ~4.8 for all the AAVs. The VP1/2 common region had some variability in calculated pI value across the AAV serotypes ranging from ~5.2 (AAV11) to ~9.8 (AAV7, AAV8, and AAV10). This variability was likely due to the lower number of amino acids used for the calculation than that for the VP1u and VP3 sequence lengths. The average calculated pI value of the VP1/2 common

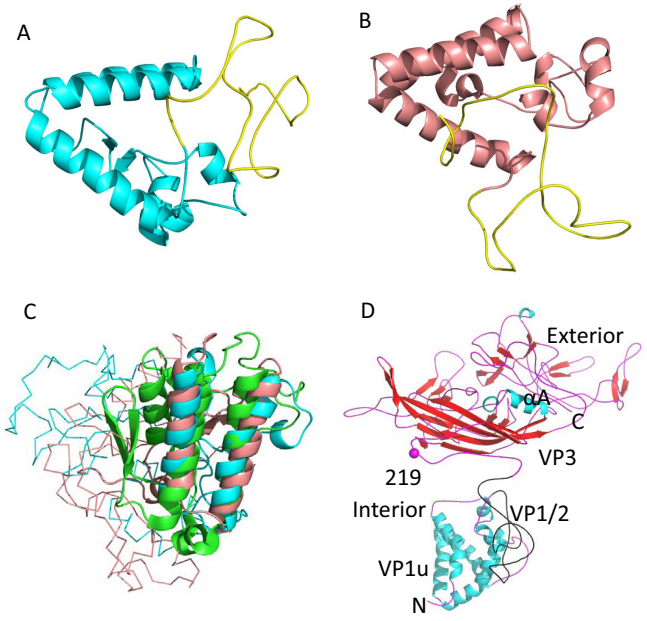

FIG 2 Cartoon rendition of VP1u models generated by Robetta. (A and B) Portions of two models of the VP1/2 sequence showing the predominantly α-helical structure of VP1u (cyan and salmon) and a stretch of the random loops in the VP1/2 common region (yellow). (C) Superposition of two models (portions of which are shown in panels A and B) onto bovine pancreatic PLA_2 (green) (PDB ID, 1BP2). The structures are superimposed with RMSDs of 3.3 Å and 2.8 Å, respectively. The active-site α-helix is conserved in both models. (D) Superposition of a model generated for AAV1 residues 1 to 250 onto the AAV1 VP3 crystal structure (residues 218 to 736). Helical regions are shown in cyan, and β-strand regions are shown in red ribbon. The VP regions are indicated, the Cα position of residue 219 is indicated with a purple sphere, αA is labeled, and the interior and exterior surfaces of the VP are indicated. These images were generated using PyMOL (DeLano Scientific).

region across the serotypes was ~7.2. The VP3 sequences had an average calculated pI value of ~6.3. Empty capsids also have a mean calculated pI value of ~6.3 for all the AAVs, likely due to the high abundance of VP3 in the capsid (1:1:10 for VP1:VP2:VP3). This value was comparable to the previous experimentally determined value for AAV1 (63). The accepted pI value for DNA (nucleotides) from the literature is ~5.0 (58). Using this information, the AAV capsids with packaged genomes (~4.7 kb) had an average calculated pI value of ~5.9, a difference of ~0.4 compared to empty capsids.

Solution studies reveal an ordered structural state for the AAV1 and AAV6 VP1u. Intact VLPs or empty capsids were used in the CD experiments. The CD spectrum of AAV1 VLPs at pH 7.5 and 30°C was dominated by an ordered α-helical secondary structure signal with a deconvoluted helical content of 35 to 45% (Fig. 5; Table 1). Of the 518 VP3 common residues ordered in the AAV1 crystal structure, the largest helical region is the 3-turn conserved α-helix (αA, residues 294 to 303; Fig. 1A and 2D), which contributes 1.9% of the total secondary structure of the ordered VP3 monomer. Two other smaller stretches of helical structure (4 and 5 residues each) are observed in the VP3 monomer structure, accounting for 1.7% of the total secondary structure. These regions thus account for ~3.6% of the α-helical content of VP3 and ~3.4% of the α-helical content of the capsid. Therefore, the majority of the capsid α-helical signal observed in solution must be due to a region of the capsid VP that was not observed in the crystal structure, residues 1 to 217. This includes VP1u (residues 1 to 137), the VP1/2 N-terminal common region, and the first 15 N-terminal residues of the VP1/VP2/VP3 common region. However, given the Robetta models and the PONDR-Fit data described above, it is most likely that the α-helical signal arises from the VP1u sequence.

In order to observe thermal transitions in the secondary structure of the VLPs, CD spectra were collected for the AAV1 VLPs between the temperatures of 30 and 90°C. As the temperature was increased from 30 to 90°C, the CD spectra for AAV1 showed a loss of α-helical secondary structure at ~70°C (Fig. 5), while electron micrographs showed that the capsids were still intact at a similar temperature (Fig. 6). This would suggest that the changes seen in the CD signal were primarily a local denaturation event of the VPs rather than whole-capsid degradation. In order to measure the thermal transition temperature for this loss of α-helicity, ellipticity values at 208 nm were plotted against temperature for the CD data collected at different pHs (Fig. 7 and 8). For the data collected at pH 7.5 and 6.0, two distinct conformational states were observed, and the midpoint between these two states was taken as the thermal transition temperature (Table 1). At pH 5.5 and 4.0, the ellipticity values were uniformly low with no obvious transition as the temperature was increased. This suggests an already transitioned state at the low pHs.

In order to understand the effect of endosomal and lysosomal pH values on the secondary structural state of the AAV1 VLPs, CD spectra collected at different pHs,7.5, 6, 5.5, and 4.0, at 30°C were compared. The spectra obtained at the different pHs showed different secondary structural characteristics (Fig. 8). The AAV1 CD spectrum at pH 6.0 showed a definite decrease in the degree of α-helicity compared to the spectrum at pH 7.5. This trend continued at pHs 5.5 and 4.0 with significant reduction in CD signal at the lowest pH. Electron microscopy images of the capsids at these acidic pHs showed no loss of integrity, consistent with crystal structures determined at the different endosomal pHs for AAV1 (Edward Miller and Mavis Agbandje-McKenna, unpublished data) and AAV8 (54). To determine if the conformational change observed was reversible, AAV1 VLPs were treated at pH 4.0 and then buffer exchanged back to pH 7.5 prior to CD data collection. The α-helical signal was restored (Fig. 8). Negative-stain EM confirmed that these capsids were also intact (not shown). Thus, the structural transitions that occur with decrease in pH from 7.5 to 4.0 do not affect the overall capsid integrity and are reversible, including the restoration of the α-helical content at pH 7.5. These observations suggest that the conformational changes may be controlled by the differential pI of the VP domains (Fig. 4) and indicate that a decrease in pH may serve as a mechanism to destabilize the capsid or make it more flexible. The observation that the capsid integrity was maintained at the low pHs indicates that the change in CD signal under these conditions must be arising from a region of the VP that does not participate in capsid assembly, with VP1u the most likely candidate.

In order to confirm that the AAV1 VLP α-helical signal, which decreases with pH and increasing temperature, is due mostly to the VP1u region, CD spectra were collected for capsids of the closely related AAV6 (which differs from AAV1 by 6 amino acids) lacking the VP1u region. AAV6 was used for these studies because a construct of AAV1 lacking VP1 is currently not available. CD spectra were collected at pH 7.5 on AAV6 VLPs and empty capsids

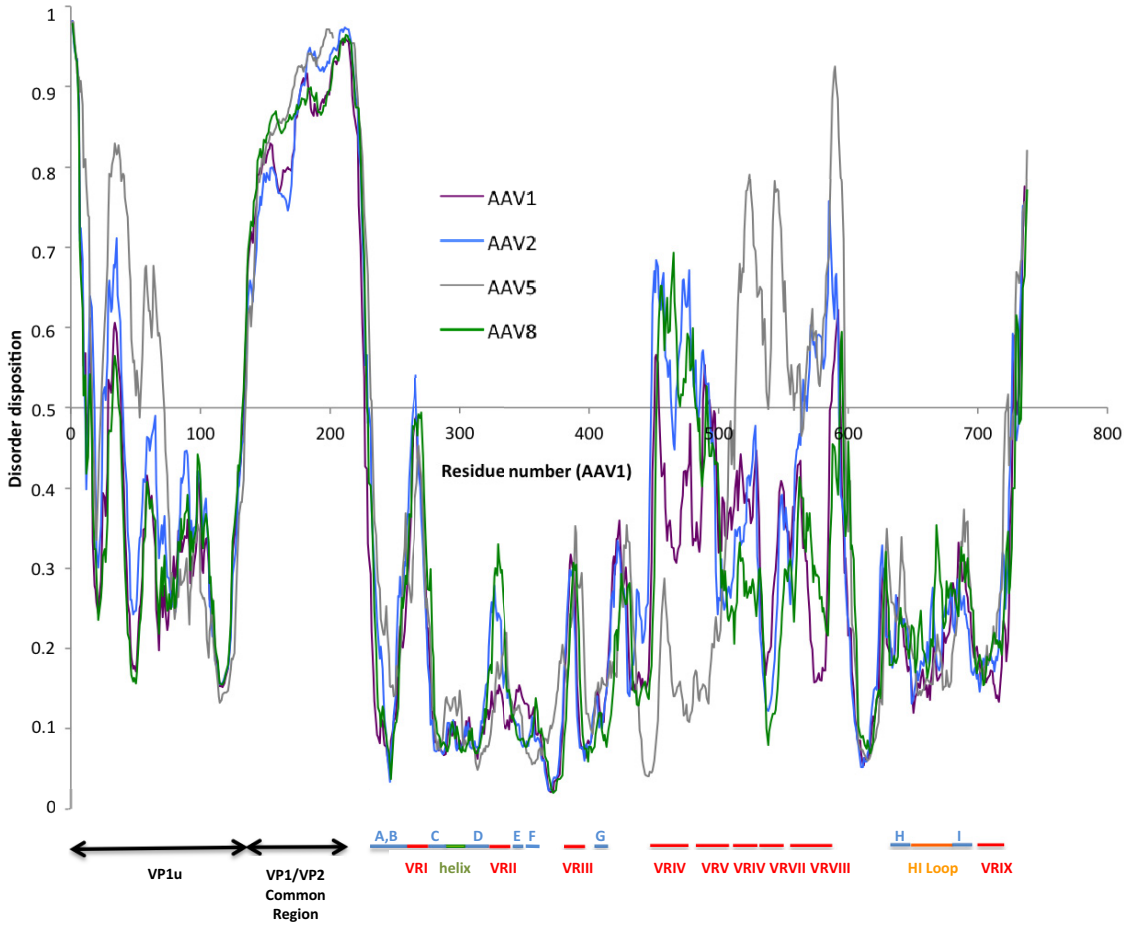

FIG 3 PONDR-Fit plot of AAV1, AAV2, AAV5, and AAV8 VP1 sequences. The plot shows the disorder disposition (*y* axis) plotted against the residue number (*x* axis). The secondary-structure assignments (blue indicates β-strands, and green indicates αA) of the crystal structures of these viruses are shown below the *x* axis along with the regions designated as being variable (VRs VRI to VRIX, in red) between the AAVs. The residues within the HI loop located on the floor of the capsid surface depression surrounding the icosahedral 5-fold axis are also indicated. Common regions of intrinsic disorder (disorder disposition of >0.5) and order (<0.5) are observed for the four serotypes compared, although the degree of disorder differs in the VR regions.

assembled from VP1, VP2, and VP3 as well as VLPs assembled from VP2 and VP3 only (Fig. 9). As observed for AAV1, the AAV6 VLP spectra were dominated by the α-helical signal. It showed a significant reduction (~50%) in the intensity of the CD signal at pH 7.5 when VP1 was absent. Significantly, the AAV6 VP1, VP2, and VP3 VLPs were generated from two baculovirus constructs, one carrying the gene for VP1 and the other encoding VP2 and VP3. Thus, the observed decrease in CD signal in the VP2 and VP3 VLPs can be confidently assigned to the lack of VP1. Given the intrinsic disorder predicted for the VP1/2 overlapping region, the increased signal for the VP1-, VP2-, and VP3-containing VLPs and empty capsids can be interpreted as arising from VP1u. The α-helical signal for the VP2 and VP3 VLPs compared to the VP1, VP2, and VP3 VLPs was reduced by 50% (Fig. 9), while that for AAV1 incubated at pH 5.5 and 4.0 was reduced by ~70% and 80% (Fig. 8), respectively, compared to its signal at pH 7.5. This is consistent with a contribution from helical regions within VP3, for example, αA and other smaller stretches of α-helix, to the signal observed at pH 7.5. The CD spectra for the VP1, VP2, and VP3 VLPs and empty capsids were similar in intensity and shape. This thus further confirms previous reports that AAV and other parvovirus capsids assembled in heterogonous systems, such as the baculovirus/Sf9 system, are identical to those produced in mammalian systems. A temperature profile for the AAV6 VP1, VP2, and VP3 VLPs, with data collected between 30 and 90°C, showed the same trend as for the AAV1 VLPs, with a decrease in the α-helical signal with increasing temperature (data not shown).

DISCUSSION

The exact reasons for the lack of ordered electron density for VP1u, the VP1/2 N-terminal region, and the first ~15 residues of the VP1/VP2/VP3 common sequence in crystal structures of the AAVs and other parvovirus capsids are unknown. The PONDR-Fit (59) program predicted a high level of intrinsic disorder in the AAV VP1/2-common (residues 138 to 202) and VP1/VP2/VP3 common N-terminal regions (up to ~220) and an ordered structural state for the VP1u. The intrinsic disorder predicted for the VP1/VP2 common residues and the first ~15 residues of VP3 would explain why these residues are not ordered in crystal structures, besides their low copy numbers not being compatible with the icosahedral averaging process used during structure determination. In the case of VP1u, since the VP1/2 common region

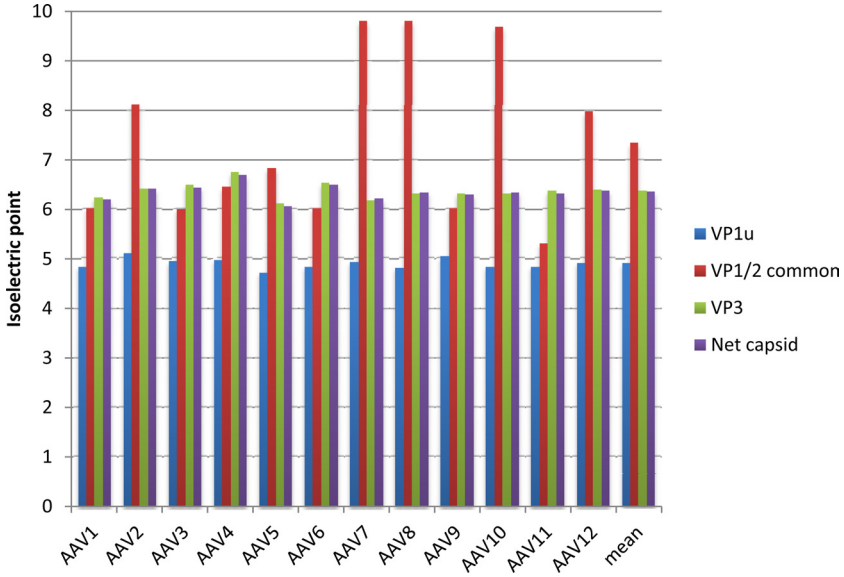

FIG 4 Calculated pI values for AAV1 to AAV12. The histogram of the pI values for the AAV serotypes shows that different capsid sequences have different electrostatic properties. The VP1u (blue) pI values are 1 unit lower than the average pI values of VP3 (green) and the whole (net) capsid (purple). The VP1/2 common region (red) shows a variable pI among the different serotypes.

would act as a connector, a "flexible hinge," to the ordered VP1/VP2/VP3 common residues, the flexibility of the connector may lead to lack of density for this region in averaged crystal structures. Consistent with the PONDR-Fit prediction, the Robetta server produced models with an ordered α-helical propensity for the AAV1 VP1u and loop structure for the VP1/VP2/VP3 common N-terminal regions. Significantly, the location of VP1u under the icosahedral 2-fold axis following the superposition of the Robetta models onto the AAV1 crystal structure was consistent with previous cryo-EM studies reporting density globules in this region predicted to be VP1u and not observed in capsids assembled with only VP2 and VP3 (27, 64).

The CD experiments served as a method to confirm that there is a significant amount of detectable ordered α-helical region in the AAV1 capsid that is likely attributable to the VP1u. This was confirmed using AAV6 VLPs and empty capsids that showed that a substantial amount of α-helical CD signal can be attributed to the VP1u region (Fig. 9). Previous reports show PLA_2 protein structures from bovine pancreas (62), snake (65), and bee (66) venom to be primarily α-helical. Thus, since VP1u also contains a PLA_2 domain, it is perhaps not surprising that an ordered α-helical propensity is predicted for it. The α-helical content of the AAV1 capsid, assuming 5 VP1s, 5 VP2s, and 50 VP3s, is ~4.5%, with the VP1u model helices accounting for ~1.1%, the VP1/VP2/VP3 common αA accounting for ~1.9%, and two small stretches of helical structure in the loops between the β-strands accounting for the remainder. These helical secondary structure percentages are much lower than the helical content estimated from the CD data for the AAV1 capsid at pH 7.5 and lower (Table 1). However, high estimates of helical content based on deconvoluted CD spectra are common due to the fact that the spectra are more sensitive to α-helical than to beta or random coil secondary structural elements. The sensitivity of CD spectra to α-helical regions was evident in the AAV6 VLP comparison, with the VP2 and VP3 VLP spectra showing a 50% decrease in the CD signal compared to the VP1, VP2, and VP3 VLPs, while VP1u should be contributing only approximately a quarter of the CD signal based on the percentages above. If only the VP1u models are considered, their average α-helical content is ~53% when folded. A 50% contribution from this region to the CD signal would close the gap

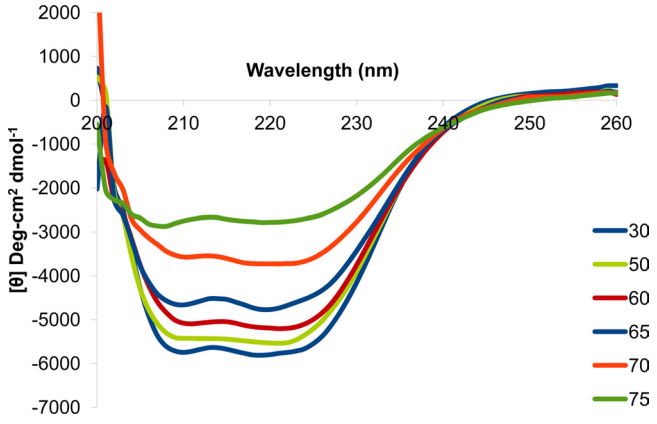

FIG 5 Representative CD spectra of AAV1 VLPs at different temperatures. A clear α-helical propensity can be seen for AAV1. This helical signal (proposed to be due mostly to VP1u) is lost as temperature increases: 30°C (blue), 50°C (lime green), 60°C (red), 65°C (navy blue), 70°C (orange), and 75°C (green).

TABLE 1 Percentage of α-helicity and transition temperatures for AAV1 VLPs from deconvoluted CD spectra data collected at different pHs[a]

pH	α-Helicity (%)	Structural transition temp ± SE (°C)
7.5	35–45	72 ± 3
6.0	25–35	63 ± 2
5.5	<10	ID
4.0	<10	ID

[a] Values based on triplicate experiments; ID, indeterminate value.

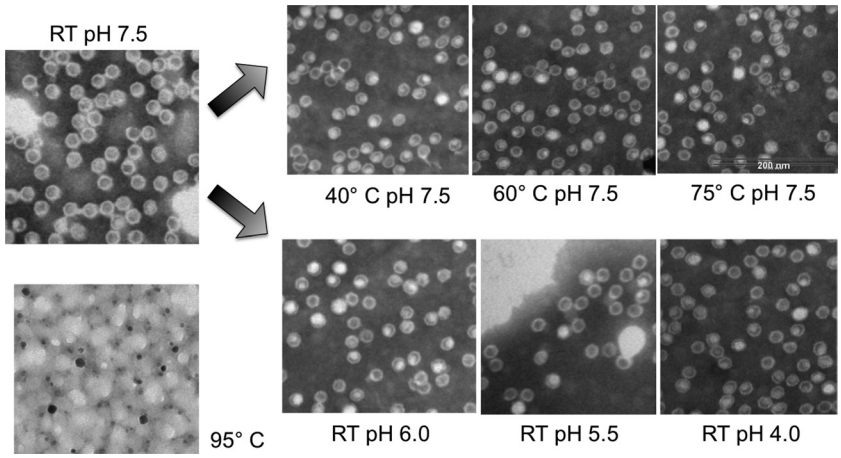

FIG 6 Electron micrographs of the AAV1 VLPs. At the different temperatures and pHs used for the CD experiments, the capsids are still intact. Only when heated to 95°C do the capsids show complete denaturation. The images were collected at a magnification of ×50,000. RT, room temperature.

between the percentages deconvoluted from the spectra collected at pH 7.5 and 6.0 and those calculated based on the VP3 structure and VP1u models. These CD data thus represent the first experimental documentation of a pH-induced change in α-helical secondary structure in any parvovirus, which is predicted to be due to VP1u structural transitions.

Previous studies have shown that heating the AAV capsid to a temperature of ~70°C results in the irreversible externalization of the VP1u region (44, 64). While high temperature may not be the biological cause for VP1u exposure during the infective pathway of the virus, this study shows that exposure of the capsid to pHs that mimic endosomal compartments results in structural changes in the VP1u similar to those seen at high temperatures. The negative-stain EM at different temperatures and pHs and crystal structure data for AAV1 (Edward Miller and Mavis Agbandje-McKenna, unpublished) and AAV8 (54) showed that the capsid integrity was intact and the mostly β-strand structure of the VP3 common region was unperturbed by pH, respectively. The conserved αA structure is also maintained in these low-pH structures. Thus, the loss of the α-helical signal at high temperature (~70°C) (Fig. 5) and low pH (5.5 and 4.0) is assumed to represent the unfolding of the secondary structure of the VP1u and is predicted to have a role in the externalization process. This may explain how high temperatures are able to induce exposure of the VP1u, by inducing first the unfolding of the VP1u region and then its externalization. While a decrease in pH (to ~5.0) has not been shown to induce significant capsid surface exposure of VP1u (44), this study shows that there is a pH-induced structural change that takes place in the capsid. It is possible that previous reports of the inability of pH changes to induce VP1u externalization *in vitro*, based on antibody assays, were affected by altered antibody binding ability at low pHs. The goal of this study was not to document externalization of VP1u but rather to document the VP dynamics that could facilitate such a process.

The pH-induced unfolding of VP1u would be an important step in the externalization process in addition to other biological or chemical factors. A factor that may contribute to VP1u unfolding relative to the other VP regions and subsequent externaliza-

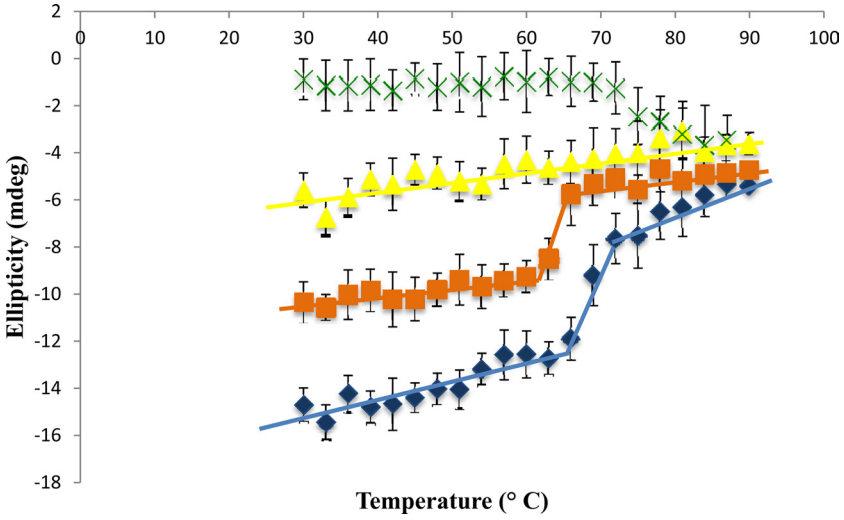

FIG 7 Temperature transition curves for AAV1 VLPs at different pHs based on CD signals at 208 nm. Plots are shown for pH 7.5 (dark blue), pH 6.0 (orange), pH 5.5 (yellow), and pH 4.0 (green). mdeg, millidegrees.

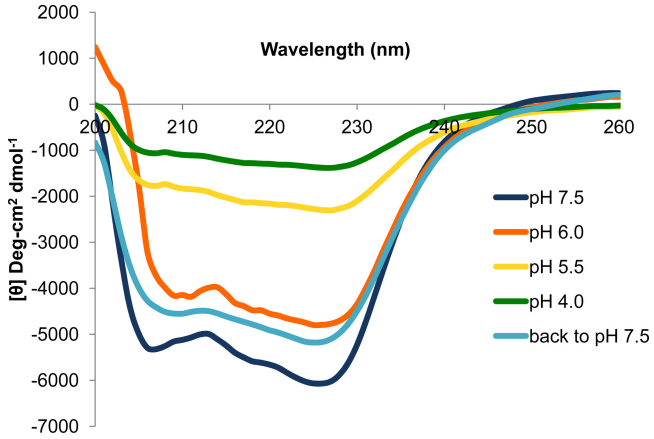

FIG 8 Representative CD spectra of AAV1 VLPs at the different pHs collected at 25°C. Plots are shown for pH 7.5 (dark blue), pH 6.0 (orange), pH 5.5 (yellow), pH 4.0 (green), and pH 4.0 to 7.5 (blue). A loss of secondary structure is seen with decrease in pH. This signal is restored when the pH 4.0 sample is transitioned back to pH 7.5.

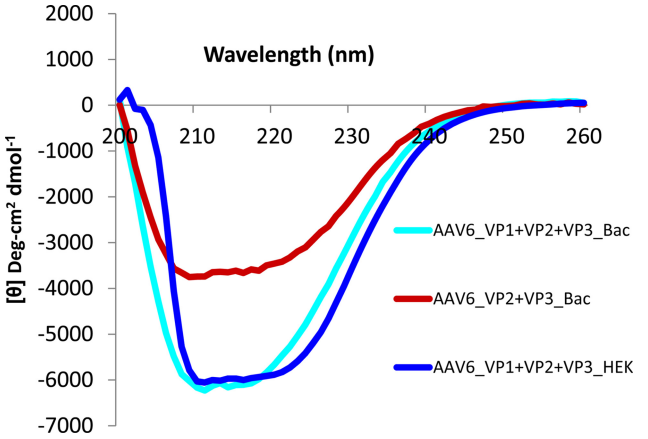

FIG 9 Representative CD spectra of AAV6 VLPs and empty capsids at pH 7.5. Plots are shown for VLPs and empty capsids assembled from VP1, VP2, and VP3 (cyan and blue) and VLPs assembled from VP2 and VP3 only (red). A decrease in α-helical propensity (~50%) is seen in the VLPs assembled from VP2 and VP3 only.

tion is its local low pI value, which is lower than those of the other capsid VP regions and the overall capsid, including the packaged genome. An analysis of the calculated pI values of different capsid regions for AAV serotypes 1 to 12 showed that VP1u has an acidic character, with pI values for all the AAVs of ~4.8. The pI for the VP1/2 common region showed more variability, with value ranges from ~5.2 to ~9.8 across the 12 serotypes, but the mean value (~7.2) was more basic than the VP3 sequence/capsid at 6.3. The VP3 and net capsid pI values at 6.3 would indicate that they would be in a zwitterionic state under early-to-late endosomal pHs, ~5.5 to 6.5, although at pH 5.5 residues in the capsid interior, including histidines observed to contact ordered DNA (54), would become protonated while VP1u and DNA, at pIs of ~4.8 and ~5.0, respectively, would still be negatively charged. This difference might be a determinant factor of the VP1u-specific structural changes at the low pHs of the late endosome and lysosome, while the capsid itself, assembled from the VP3 common VP region, does not undergo secondary structure changes. The observed decrease in CD signal, attributed to VP1u unfolding, starts to occur at pH 5.5 and is slightly further reduced when the pH is dropped to 4.0 (Fig. 8). It is thus possible that charge-charge repulsion between the interior capsid residues and VP1u and the DNA as the environmental pH decreases may play a role in triggering VP1u unfolding and externalization. Given the large variability in the calculated pI values for the VP1/VP2 common region across the AAV serotype, it is difficult to predict how the charge state of this domain contributes to VP1u externalization. However, its flexibility, based on its predicted intrinsic disorder state, would be required to permit a large motion of VP1u for extrusion from the capsid.

Given that VP1u is ordered in solution while located inside the capsid, it becomes more difficult to visualize the process of externalization while the capsid stays intact. Biochemical studies of AAV trafficking suggest that the VP1u and VP1/VP2 common N termini become externalized, from an intact capsid, in the endosomal compartment prior to entry into the cytoplasm (44). Mutagenesis studies altering residues at the base of and within the 5-fold channel formed by symmetry-related DE loops have suggested this pore as the route for VP1u externalization (45). However, in structural studies of AAV8 capsids at different pHs, only a minor increase in diameter, <1.0 Å, was observed at the top of this channel when the pH was shifted from 7.5 to 4.0 (54). For AAV1, the top of the pore is ~1.5 Å wider at pH 4.0 than at pH 7.5 (Edward Miller and Mavis Agbandje-McKenna, unpublished). In both viruses, these differences are not propagated down into the channel, which is ~20 Å in diameter at the top and ~12 Å at its base. This is too narrow to allow a folded VP1u to be threaded through, consistent with reports that pH alone likely does not lead to VP1u externalization (44). In a more recent study, it was reported that formation of dityrosine adducts across the 2-fold axis, which generated cross-linked dimers, prevented externalization of the VP1u (67). This observation led to the suggestion that capsid dynamics at the 2-fold axis may also be involved in VP1u externalization. However, as with the 5-fold axis, the low-pH structures of AAV1 and AAV8 showed no major structural rearrangements at the 2-fold axis that would enable VP1u externalization. Only side chain conformational changes are observed. These structural observations thus invoke the likely involvement of other factors in this process. In a study by Levy et al. on AAV2 complexed with heparin, a structural change was reported at the 5-fold channel in the presence of this cell surface glycan receptor (68). The channel was reported to open in an iris-like rotation of the ring of residues leading to the widening of the top. However, the widening was also not enough to allow a folded VP1u to be externalized. Thus, it is possible that receptor attachment or other cellular interactions or conditions, combined with endosomal acidification, may precede the unfolding of VP1u in the context of endosomal trafficking of the capsid. It is also possible that the completely unfolded VP1u can thread through an unexpanded 5-fold channel.

The CD data can be combined with models generated by Robetta for the VP1u and VP1/2 sequence and confirmatory structure prediction from the PONDR-Fit algorithm to generate a pH-induced unfolding, externalization through the 5-fold channel, and refolding model for VP1u and VP1/2 (Fig. 10). In this model, VP1u, with a reversible unfolding/folding phenotype (Fig. 8), would adopt a native structure following externalization into a favorable environment. However, it is difficult to reconcile the

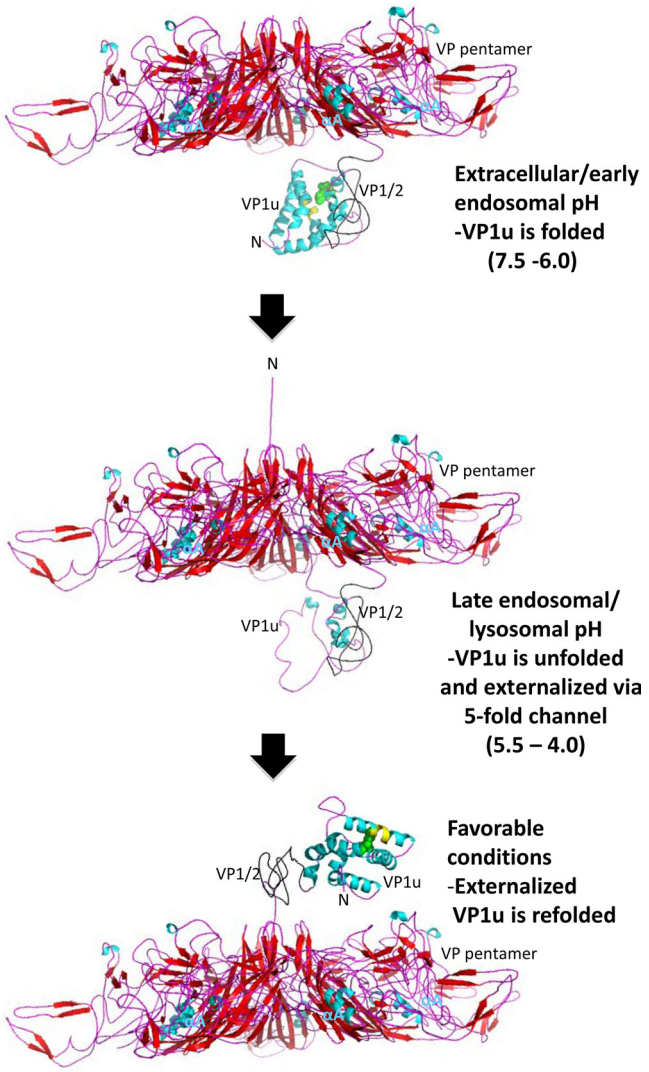

FIG 10 AAV VP1u externalization model. A VP pentamer containing one VP1 and 4 VP3s is shown, in which the model of VP residues 1 to 250, superposed onto the AAV1 VP3 crystal structure (1NG9) monomer, is localized directly beneath the 5-fold and 2-fold interfaces. At pH 7.5 or 6.0, the VP1u is folded. As pH is decreased to 5.5 and 4.0, unfolding is initiated and the VP1u and VP1/VP2 common region are subsequently threaded through the 5-fold pore. When the correct conditions are encountered, possibly via the lipid membrane or substrate, refolding of the partially or completely unfolded VP1u to the native functional state occurs. The PLA_2 active site and Ca^{2+} binding residues are shown in yellow and green, respectively. The images were generated using PyMOL (DeLano Scientific).

externalization of an unfolded VP1u in the late endosome or lysosome with its PLA_2 function to enable escape from these cellular compartments when this activity is reported to have a pH optimum of 7.0 (69). Reports on AAV2 trafficking have indicated that capsids can escape from early endosomes (43, 44). At this pH (~6.0), the VP1u would be mostly folded with some PLA_2 activity, although it is not obvious how it would escape from its interior location, inside the capsid. Under late endosomal conditions, pH ~5.5, it is possible that VP1u is only partially unfolded, retains some of its function, and on contact with its substrate on the lipid membrane, becomes fully functional. The same could be true for escape at pH 4.0, although functionality would be expected to be more severely impaired at this pH. These possibilities require further study.

In summary, AAV1 and AAV6 VP1u are structurally ordered in an α-helical conformation inside the capsid. This secondary structure is reversibly unfolded/refolded in a pH-dependent manner by decrease in pH from 7.5 to 4.0 and increase back to 7.5. A predicted intrinsic disorder in the VP1/2 common region and the differential charge states of the VP1u and the VP3 capsid likely impart the flexibility and repulsion, respectively, required to permit the externalization of VP1u through the 5-fold channel following low-pH-induced unfolding in the low pH of the late endosomal (~5.5) or lysosomal (4.0) compartments. It is also possible that the 2-fold axis plays a role in this externalization process. This study provides insights into the potential mechanism of capsid VP rearrangements in preparation for endosomal escape of the AAV capsid.

ACKNOWLEDGMENTS

This project was funded by grants from NIH projects R01 AI081961 (M.A.-M., B.B., R.M., and N.M.), NIH R01 GM082946 and P01 HL59412 (M.A.-M., R.M., and N.M.), and NIH R01 AI072176 (M.A.-M. and R.J.S.). B.V. was partially supported by University of Florida Alumni and Grinter Fellowships. J.Y. was supported by the HHMI Science for Life program.

REFERENCES

1. **Atchison RW, Casto BC, Hammon WM.** 1965. Adenovirus-associated defective virus particles. Science **149**:754–755.
2. **Buller RML, Janik JE, Sebring ED, Rose JA.** 1981. Herpes simplex virus types 1 and 2 completely help adenovirus-associated virus replication. J. Virol. **40**:241–247.
3. **Geoffroy M-C, Salvetti A.** 2005. Helper functions required for wild type and recombinant adeno-associated virus growth. Curr. Gene Ther. **5**:265–271.
4. **Walz C, Deprez A, Dupressoir T, Dürst M, Rabreau M, Schlehofer JR.** 1997. Interaction of human papillomavirus type 16 and adeno-associated virus type 2 co-infecting human cervical epithelium. J. Gen. Virol. **78**(Part 6):1441–1452.
5. **Gao G, Vandenberghe LH, Alvira MR, Lu Y, Calcedo R, Zhou X, Wilson JM.** 2004. Clades of adeno-associated viruses are widely disseminated in human tissues. J. Virol. **78**:6381–6388.
6. **Mori S, Wang L, Takeuchi T, Kanda T.** 2004. Two novel adeno-associated viruses from cynomolgus monkey: pseudotyping characterization of capsid protein. Virology **330**:375–383.
7. **Schmidt M, Voutetakis A, Afione S, Zheng C, Mandikian D, Chiorini JA.** 2008. Adeno-associated virus type 12 (AAV12): a novel AAV serotype with sialic acid- and heparan sulfate proteoglycan-independent transduction activity. J. Virol. **82**:1399–1406.
8. **Burger C, Gorbatyuk OS, Velardo MJ, Peden CS, Williams P, Zolotukhin S, Reier PJ, Mandel RJ, Muzyczka N.** 2004. Recombinant AAV viral vectors pseudotyped with viral capsids from serotypes 1, 2, and 5 display differential efficiency and cell tropism after delivery to different regions of the central nervous system. Mol. Ther. **10**:302–317.
9. **Davidson BL, Stein CS, Heth JA, Martins I, Kotin RM, Derksen TA, Zabner J, Ghodsi A, Chiorini JA.** 2000. Recombinant adeno-associated virus type 2, 4, and 5 vectors: transduction of variant cell types and regions in the mammalian central nervous system. Proc. Natl. Acad. Sci. U. S. A. **97**:3428–3432.
10. **Gao G-P, Alvira MR, Wang L, Calcedo R, Johnston J, Wilson JM.** 2002. Novel adeno-associated viruses from rhesus monkeys as vectors for human gene therapy. Proc. Natl. Acad. Sci. U. S. A. **99**:11854–11859.
11. **Kaludov N, Brown KE, Walters RW, Zabner J, Chiorini JA.** 2001. Adeno-associated virus serotype 4 (AAV4) and AAV5 both require sialic acid binding for hemagglutination and efficient transduction but differ in sialic acid linkage specificity. J. Virol. **75**:6884–6893.
12. **Rabinowitz JE, Rolling F, Li C, Conrath H, Xiao W, Xiao X, Samulski RJ.** 2002. Cross-packaging of a single adeno-associated virus (AAV) type 2

vector genome into multiple AAV serotypes enables transduction with broad specificity. J. Virol. **76**:791–801.
13. **Walters RW, Yi SMP, Keshavjee S, Brown KE, Welsh MJ, Chiorini JA, Zabner J.** 2001. Binding of adeno-associated virus type 5 to 2,3-linked sialic acid is required for gene transfer. J. Biol. Chem. **276**:20610–20616.
14. **Maguire AM, Simonelli F, Pierce EA, Pugh EN, Mingozzi F, Bennicelli J, Banfi S, Marshall KA, Testa F, Surace EM, Rossi S, Lyubarsky A, Arruda VR, Konkle B, Stone E, Sun J, Jacobs J, Dell'Osso L, Hertle R, Ma J, Redmond TM, Zhu X, Hauck B, Zelenaia O, Shindler KS, Maguire MG, Wright JF, Volpe NJ, McDonnell JW, Auricchio A, High KA, Bennett J.** 2008. Safety and efficacy of gene transfer for Leber's congenital amaurosis. N. Engl. J. Med. **358**:2240–2248.
15. **Buller RM, Rose JA.** 1978. Characterization of adenovirus-associated virus-induced polypeptides in KB cells. J. Virol. **25**:331–338.
16. **Johnson FB, Ozer HL, Hoggan MD.** 1971. Structural proteins of adenovirus-associated virus type 3. J. Virol. **8**:860–863.
17. **Rose JA, Maizel JV, Inman JK, Shatkin AJ.** 1971. Structural proteins of adenovirus-associated viruses. J. Virol. **8**:766–770.
18. **Lerch TF, Xie Q, Chapman MS.** 2010. The structure of adeno-associated virus serotype 3B (AAV-3B): insights into receptor binding and immune evasion. Virology **403**:26–36.
19. **Miller EB, Gurda-Whitaker B, Govindasamy L, McKenna R, Zolotukhin S, Muzyczka N, Agbandje-McKenna M.** 2006. Production, purification and preliminary X-ray crystallographic studies of adeno-associated virus serotype 1. Acta Crystallogr. Sect. F Struct. Biol. Cryst. Commun. **62**:1271–1274.
20. **DiMattia MA, Nam HJ, Van Vliet K, Mitchell M, Bennett A, Gurda BL, McKenna R, Olson NH, Sinkovits RS, Potter M, Byrne BJ, Aslanidi G, Zolotukhin S, Muzyczka N, Baker TS, Agbandje-McKenna M.** 2012. Structural insight into the unique properties of adeno-associated virus serotype 9. J. Virol. **86**:6947–6958.
21. **Nam H-J, Lane MD, Padron E, Gurda B, McKenna R, Kohlbrenner E, Aslanidi G, Byrne B, Muzyczka N, Zolotukhin S, Agbandje-McKenna M.** 2007. Structure of adeno-associated virus serotype 8, a gene therapy vector. J. Virol. **81**:12260–12271.
22. **Ng R, Govindasamy L, Gurda BL, McKenna R, Kozyreva OG, Samulski RJ, Parent KN, Baker TS, Agbandje-McKenna M.** 2010. Structural characterization of the dual glycan binding adeno-associated virus serotype 6. J. Virol. **84**:12945–12957.
23. **Padron E, Bowman V, Kaludov N, Govindasamy L, Levy H, Nick P, McKenna R, Muzyczka N, Chiorini JA, Baker TS, Agbandje-McKenna M.** 2005. Structure of adeno-associated virus type 4. J. Virol. **79**:5047–5058.
24. **Quesada O, Gurda B, Govindasamy L, McKenna R, Kohlbrenner E, Aslanidi G, Zolotukhin S, Muzyczka N, Agbandje-McKenna M.**2007. Production, purification and preliminary X-ray crystallographic studies of adeno-associated virus serotype 7. Acta Crystallogr. Sect. F Struct. Biol. Cryst. Commun. **63**:1073–1076.
25. **Walters RW, Agbandje-McKenna M, Bowman VD, Moninger TO, Olson NH, Seiler M, Chiorini JA, Baker TS, Zabner J.** 2004. Structure of adeno-associated virus serotype 5. J. Virol. **78**:3361–3371.
26. **Xie Q, Bu W, Bhatia S, Hare J, Somasundaram T, Azzi A, Chapman MS.** 2002. The atomic structure of adeno-associated virus (AAV-2), a vector for human gene therapy. Proc. Natl. Acad. Sci. U. S. A. **99**:10405–10410.
27. **Kronenberg S, Böttcher B, von der Lieth CW, Bleker S, Kleinschmidt JA.** 2005. A conformational change in the adeno-associated virus type 2 capsid leads to the exposure of hidden VP1 N termini. J. Virol. **79**:5296–5303.
28. **Sonntag F, Köther K, Schmidt K, Weghofer M, Raupp C, Nieto K, Kuck A, Gerlach B, Böttcher B, Müller OJ, Lux K, Hörer M, Kleinschmidt JA.** 2011. The assembly-activating protein promotes capsid assembly of different adeno-associated virus serotypes. J. Virol. **85**:12686–12697.
29. **Agbandje-McKenna M, Kleinschmidt J.** 2011. AAV capsid structure and cell interactions. Methods Mol. Biol. **807**:47–92.
30. **Bell CL, Vandenberghe LH, Bell P, Limberis MP, Gao G-P, Van Vliet K, Agbandje-McKenna M, Wilson JM.** 2011. The AAV9 receptor and its modification to improve in vivo lung gene transfer in mice. J. Clin. Invest. **121**:2427–2435.
31. **Dickey DD, Excoffon KJDA, Koerber JT, Bergen J, Steines B, Klesney-Tait J, Schaffer DV, Zabner J.** 2011. Enhanced sialic acid-dependent endocytosis explains the increased efficiency of infection of airway epithelia by a novel adeno-associated virus. J. Virol. **85**:9023–9030.
32. **Shen S, Bryant KD, Brown SM, Randell SH, Asokan A.** 2011. Terminal N-linked galactose is the primary receptor for adeno-associated virus 9. J. Biol. Chem. **286**:13532–13540.
33. **Summerford C, Samulski RJ.** 1998. Membrane-associated heparan sulfate proteoglycan is a receptor for adeno-associated virus type 2 virions. J. Virol. **72**:1438–1445.
34. **Wu Z, Asokan A, Grieger JC, Govindasamy L, Agbandje-McKenna M, Samulski RJ.** 2006. Single amino acid changes can influence titer, heparin binding, and tissue tropism in different adeno-associated virus serotypes. J. Virol. **80**:11393–11397.
35. **Wu Z, Miller E, Agbandje-McKenna M, Samulski RJ.** 2006. Alpha2,3 and alpha2,6 N-linked sialic acids facilitate efficient binding and transduction by adeno-associated virus types 1 and 6. J. Virol. **80**:9093–9103.
36. **Asokan A, Hamra JB, Govindasamy L, Agbandje-McKenna M, Samulski RJ.** 2006. Adeno-associated virus type 2 contains an integrin {alpha}5{beta}1 binding domain essential for viral cell entry. J. Virol. **80**:8961–8969.
37. **Qing K, Mah C, Hansen J, Zhou S, Dwarki V, Srivastava A.** 1999. Human fibroblast growth factor receptor 1 is a co-receptor for infection by adeno-associated virus 2. Nat. Med. **5**:71–77.
38. **Summerford C, Bartlett JS, Samulski RJ.** 1999. AlphaVbeta5 integrin: a co-receptor for adeno-associated virus type 2 infection. Nat. Med. **5**:78–82.
39. **Di Pasquale G, Davidson BL, Stein CS, Martins I, Scudiero D, Monks A, Chiorini JA.** 2003. Identification of PDGFR as a receptor for AAV-5 transduction. Nat. Med. **9**:1306–1312.
40. **Akache B, Grimm D, Pandey K, Yant SR, Xu H, Kay MA.** 2006. The 37/67-kilodalton laminin receptor is a receptor for adeno-associated virus serotypes 8, 2, 3, and 9. J. Virol. **80**:9831–9836.
41. **Uhrig S, Coutelle O, Wiehe T, Perabo L, Hallek M, Büning H.** 2012. Successful target cell transduction of capsid-engineered rAAV vectors requires clathrin-dependent endocytosis. Gene Ther. **19**:210–218.
42. **Nonnenmacher M, Weber T.** 2011. Adeno-associated virus 2 infection requires endocytosis through the CLIC/GEEC pathway. Cell Host Microbe **10**:563–576.
43. **Xiao P-J, Samulski RJ.** 2012. Cytoplasmic trafficking, endosomal escape, and perinuclear accumulation of adeno-associated virus type 2 particles are facilitated by microtubule network. J. Virol. **86**:10462–10473.
44. **Sonntag F, Bleker S, Leuchs B, Fischer R, Kleinschmidt JA.** 2006. Adeno-associated virus type 2 capsids with externalized VP1/VP2 trafficking domains are generated prior to passage through the cytoplasm and are maintained until uncoating occurs in the nucleus. J. Virol. **80**:11040–11054.
45. **Bleker S, Sonntag F, Kleinschmidt JA.** 2005. Mutational analysis of narrow pores at the fivefold symmetry axes of adeno-associated virus type 2 capsids reveals a dual role in genome packaging and activation of phospholipase A2 activity. J. Virol. **79**:2528–2540.
46. **Grieger JC, Johnson JS, Gurda-Whitaker B, Agbandje-McKenna M, Samulski RJ.** 2007. Surface-exposed adeno-associated virus Vp1-NLS capsid fusion protein rescues infectivity of noninfectious wild-type Vp2/Vp3 and Vp3-only capsids but not that of fivefold pore mutant virions. J. Virol. **81**:7833–7843.
47. **Grieger JC, Snowdy S, Samulski RJ.** 2006. Separate basic region motifs within the adeno-associated virus capsid proteins are essential for infectivity and assembly. J. Virol. **80**:5199–5210.
48. **Popa-Wagner R, Porwal M, Kann M, Reuss M, Weimer M, Florin L, Kleinschmidt JA.** 2012. Impact of VP1-specific protein sequence motifs on adeno-associated virus type 2 intracellular trafficking and nuclear entry. J. Virol. **86**:9163–9174.
49. **Bartlett JS, Wilcher R, Samulski RJ.** 2000. Infectious entry pathway of adeno-associated virus and adeno-associated virus vectors. J. Virol. **74**:2777–2785.
50. **Douar AM, Poulard K, Stockholm D, Danos O.** 2001. Intracellular trafficking of adeno-associated virus vectors: routing to the late endosomal compartment and proteasome degradation. J. Virol. **75**:1824–1833.
51. **Duan D, Yue Y, Yan Z, Yang J, Engelhardt JF.** 2000. Endosomal processing limits gene transfer to polarized airway epithelia by adeno-associated virus. J. Clin. Invest. **105**:1573–1587.
52. **Hansen J, Qing K, Srivastava A.** 2001. Adeno-associated virus type 2-mediated gene transfer: altered endocytic processing enhances transduction efficiency in murine fibroblasts. J. Virol. **75**:4080–4090.
53. **Sanlioglu S, Benson PK, Yang J, Atkinson EM, Reynolds T, Engelhardt JF.** 2000. Endocytosis and nuclear trafficking of adeno-associated virus

type 2 are controlled by Rac1 and phosphatidylinositol-3 kinase activation. J. Virol. **74**:9184–9196.
54. **Nam H-J, Gurda BL, McKenna R, Potter M, Byrne B, Salganik M, Muzyczka N, Agbandje-McKenna M.** 2011. Structural studies of adeno-associated virus serotype 8 capsid transitions associated with endosomal trafficking. J. Virol. **85**:11791–11799.
55. **Grieger JC, Choi VW, Samulski RJ.** 2006. Production and characterization of adeno-associated viral vectors. Nat. Protoc. **1**:1412–1428.
56. **Greenfield NJ, Fasman GD.** 1969. Computed circular dichroism spectra for the evaluation of protein conformation. Biochemistry **8**:4108–4116.
57. **Gasteiger E, Hoogland C, Gattiker A, Duvaud S, Wilkins MR, Appel RD, Bairoch A.** 2005. Protein identification and analysis tools on the ExPASy server, p 571–607. *In* Walker JM (ed), The proteomics protocols handbook. Humana Press, Totowa, NJ.
58. **Jordan DO.** 1955. The physical properties of nucleic acids, p 447–492. *In* Chargaff E, Davidson JN (ed), The nucleic acids. Academic Press Ltd., New York, NY.
59. **Xue B, Dunbrack RL, Williams RW, Dunker AK, Uversky VN.** 2010. PONDR-FIT: a meta-predictor of intrinsically disordered amino acids. Biochim. Biophys. Acta **1804**:996–1010.
60. **Kim DE, Chivian D, Baker D.** 2004. Protein structure prediction and analysis using the Robetta server. Nucleic Acids Res. **32**:W526–W531.
61. **Emsley P, Lohkamp B, Scott WG, Cowtan K.** 2010. Features and development of *Coot*. Acta Crystallogr. D Biol. Crystallogr. **66**:486–501.
62. **Dijkstra BW, Kalk KH, Hol WG, Drenth J.** 1981. Structure of bovine pancreatic phospholipase A2 at 1.7A resolution. J. Mol. Biol. **147**:97–123.
63. **Okada T, Nonaka-Sarukawa M, Uchibori R, Kinoshita K, Hayashita-Kinoh H, Nitahara-Kasahara Y, Takeda S, Ozawa K.** 2009. Scalable purification of adeno-associated virus serotype 1 (AAV1) and AAV8 vectors, using dual ion-exchange adsorptive membranes. Hum. Gene Ther. **20**:1013–1021.
64. **Gerlach B, Kleinschmidt JA, Böttcher B.** 2011. Conformational changes in adeno-associated virus type 1 induced by genome packaging. J. Mol. Biol. **409**:427–438.
65. **White S, Scott D, Otwinowski Z, Gelb M, Sigler P.** 1990. Crystal structure of cobra-venom phospholipase A2 in a complex with a transition-state analogue. Science **250**:1560–1563.
66. **Scott DL, Otwinowski Z, Gelb MH, Sigler PB.** 1990. Crystal structure of bee-venom phospholipase A2 in a complex with a transition-state analogue. Science **250**:1563–1566.
67. **Horowitz ED, Finn MG, Asokan A.** 2012. Tyrosine cross-linking reveals interfacial dynamics in adeno-associated viral capsids during infection. ACS Chem. Biol. **7**:1059–1066.
68. **Levy HC, Bowman VD, Govindasamy L, McKenna R, Nash K, Warrington K, Chen W, Muzyczka N, Yan X, Baker TS, Agbandje-McKenna M.** 2009. Heparin binding induces conformational changes in Adeno-associated virus serotype 2. J. Struct. Biol. **165**:146–156.
69. **Canaan S, Zádori Z, Ghomashchi F, Bollinger J, Sadilek M, Moreau ME, Tijssen P, Gelb MH.** 2004. Interfacial enzymology of parvovirus phospholipases A2. J. Biol. Chem. **279**:14502–14508.
70. **Pettersen EF, Goddard TD, Huang CC, Couch GS, Greenblatt DM, Meng EC, Ferrin TE.** 2004. UCSF Chimera—a visualization system for exploratory research and analysis. J. Comput. Chem. **25**:1605–1612.
71. **Govindasamy L, Padron E, McKenna R, Muzyczka N, Kaludov N, Chiorini JA, Agbandje-McKenna M.** 2006. Structurally mapping the diverse phenotype of adeno-associated virus serotype 4. J. Virol. **80**:11556–11570.